

Melt Pool Features Analysis Using a High Speed Coaxial Monitoring System for Laser Powder Bed Fusion of Ti-6Al-4V Grade 23

Aditi Thanki (✉ aditi.thanki@kuleuven.be)

KU Leuven

Louca Goossens

KU Leuven

Agusmian Partogi Ompusunggu

Flanders Make

Mohamad Bayat

Technical University of Denmark

Abdellatif Bey-Temsamani

Flanders Make

Brecht Van Hooreweder

KU Leuven

Jean-Pierre Kruth

KU Leuven

Ann Witvrouw

KU Leuven

Research Article

Keywords: Laser Powder Bed Fusion (LPBF), Melt pool monitoring, Spatter analysis, Keyhole porosity, Finite volume modelling, X-ray computed tomography (X-CT)

Posted Date: December 20th, 2021

DOI: <https://doi.org/10.21203/rs.3.rs-1128009/v1>

License: © ⓘ This work is licensed under a Creative Commons Attribution 4.0 International License.

[Read Full License](#)

Melt pool features analysis using a high speed coaxial monitoring system for laser powder bed fusion of Ti-6Al-4V grade 23

Aditi Thanki^{1,2,*}, Louca Goossens^{1,2,*}, Agusmian Partogi Ompusunggu³, Mohamad Bayat⁴, Abdellatif Bey-Temsamani³, Brecht Van Hooreweder^{1,2}, Jean-Pierre Kruth^{1,2}, Ann Witvrouw^{1,2}

¹ *KU Leuven, Department of Mechanical Engineering, Celestijnenlaan 300B, 3001 Heverlee, Belgium*

² *Member of Flanders Make, Leuven, Belgium*

³ *Flanders Make, Gaston Geenslaan 8, 3001 Heverlee, Belgium*

⁴ *Technical University of Denmark, Department of Mechanical Engineering, building 425, Lyngby, Denmark*

*Joint first authors.

E-mail address:

Aditi.Thanki@kuleuven.be (A. Thanki)

Louca.Goossens@kuleuven.be (L. R. Goossens)

Ann.Witvrouw@kuleuven.be (A. Witvrouw)

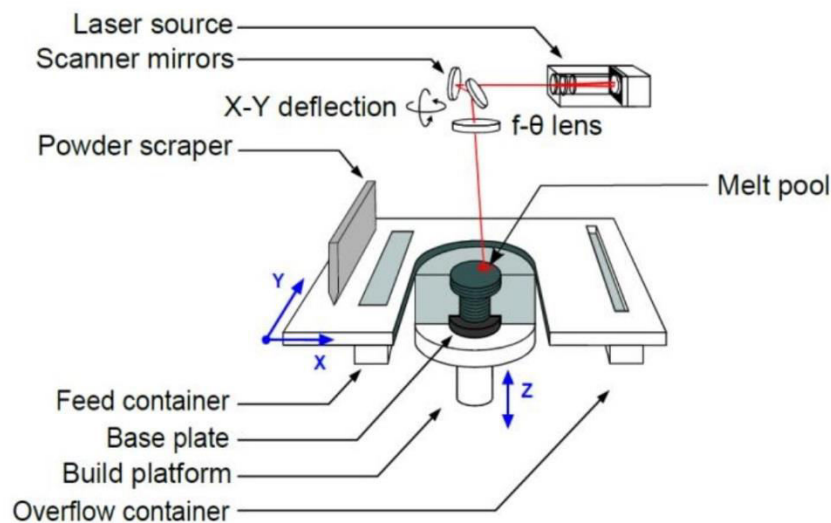
Abstract

In laser powder bed fusion (LPBF), defects such as pores or cracks can seriously affect the final part quality and lifetime. Keyhole porosity, being one type of porosity defects in LPBF, results from excessive energy density which may be due to changes in process parameters (laser power and scan speed) and/or result from the part's geometry and/or hatching strategies. To study the possible occurrence of keyhole pores, experimental work as well as simulations were carried out for optimum and high volumetric energy density conditions in Ti-6Al-4V grade 23. By decreasing the scanning speed from 1000 mm/s to 500 mm/s for a fixed laser power of 170 W, keyhole porosities are formed and later observed by X-ray computed tomography. Melt pool images are recorded in real-time during the LPBF process by using a high speed coaxial Near-Infrared (NIR) camera monitoring system. The recorded images are then pre-processed using a set of image processing steps to generate binary images. From the binary images, geometrical features of the melt pool and features that characterize the spatter particles formation and ejection from the melt pool are calculated. The experimental data clearly show spatter patterns in case of keyhole porosity formation at low scan speed. A correlation between the number of pores and the amount of spatter is observed. Besides the experimental work, a previously developed, high fidelity finite volume numerical model was used to simulate the melt pool dynamics with similar process parameters as in the experiment. Simulation results illustrate and confirm the keyhole porosity formation by decreasing laser scan speed.

Keywords: Laser Powder Bed Fusion (LPBF), Melt pool monitoring, Spatter analysis, Keyhole porosity, Finite volume modelling, X-ray computed tomography (X-CT)

39 **1. Introduction**

40 Selective laser melting (SLM), otherwise called metal laser powder bed fusion (LPBF), is a
41 process where a 3-D metal part is built in a layer-by-layer manner by utilizing a laser to melt the
42 metal powder selectively in a powder bed. Kruth and der Schueren, 1995 [1] studied this
43 technique in the mid 1990's, followed by Meiners, 1999 [2]. In this process, a thin layer of
44 metallic powder is molten at selected places by scanning a laser beam over a powder bed as per a
45 predefined scanning strategy (Figure 1). The main advantage of this process is that it enables the
46 manufacturing of complex metallic parts. Applications of the LPBF process can be found in a
47 variety of sectors. Examples of those are the medical sector [3], tool industries [4], automotive
48 industry [5] and aerospace industry [6]. The present state-of-the-art LPBF process with
49 optimized processing parameters normally leads to near or over 99% part densities. Nevertheless,
50 local defects such as pores might exist. These imperfections can be a concern as they can cause
51 variations in the mechanical properties of produced parts. The presence of these porosities
52 becomes even more problematic when the defects are present in critical zones (e.g. subject to
53 high mechanical stress) of the produced parts and thus limit the use of LPBF in critical
54 applications, such as aerospace or the medical industry. These undesirable defects might appear
55 due to non-idealities related to the processing parameter settings as well as hardware behaviour,
56 such as scanning mirror acceleration/deceleration, leading to over-melting or insufficient
57 melting.



58

59 **Figure 1.** Schematic diagram of the SLM process [7].

60 There are many reasons for pore formation in LPBF, such as lack of fusion [8], Plateau-Rayleigh
61 instability [9], overheating in overhanging structures [10] or keyhole-induced pores [11]. The
62 mechanisms behind the latter is the keyhole phenomenon, caused by high volumetric energy
63 conditions, with the resulting porosity being denoted as a keyhole pore. During keyhole mode,
64 the temperature at the centre of the laser beam and at the bottom part of the keyhole reaches
65 values above the vaporization temperature of the metal. This prompts an exponential increase in
66 the recoil pressure and a linear reduction in the surface tension, opening and stabilizing the
67 keyhole void [12]. Nevertheless, when the keyhole is dragged along during scanning, instabilities

68 can arise. Matsunawa et al., 1998 [13] showed that as a result of the keyhole front inclination
69 angle, the evaporation site can shift to different locations on the front keyhole wall. This can
70 perturb the rear melt pool wall and as a result generate instabilities and keyhole oscillation. At
71 this moment, the laser rays lose the vast majority of their energy because of multiple collisions.
72 This redistribution of the laser energy can significantly change the local temperature distribution
73 inside of the keyhole and subsequently also the local recoil pressure. With the decrease of the
74 temperature and recoil pressure, a local rise of the surface tension is observed. As a result, the
75 balance of forces is disrupted and the keyhole can no longer be sustained locally, leading to a
76 rapid collapse of the keyhole. Consequently, a gas pocket might be trapped due to the abrupt
77 breakdown of the rear wall, forming what is called a keyhole-induced pore at the bottom of the
78 keyhole.

79 Keyhole and keyhole-induced pore formation has already been studied by many authors. King et
80 al., 2014 [11] proved that under certain conditions, the melting mechanism changes from
81 conduction to keyhole mode laser melting. They identified the conditions for keyhole formation
82 through single-track experiments for 316L stainless steel. Martin et al., 2019b [14] elucidated the
83 mechanism of keyhole pore formation during laser turn points using in situ X-ray imaging and
84 multi-physics simulations. Khairallah et al., 2016 [9] developed a numerical model that included
85 the recoil pressure and the Marangoni effect and investigated the melt pool evolution. Bayat et
86 al., 2019 [12] developed a high-fidelity multiphysics numerical model taking into account multi
87 physics phenomena during LPBF. They studied the formation of keyhole porosities in printed
88 single tracks of Ti6Al4V and validated the simulation results with experimental results.
89 Cunningham et al., 2019 [15] used an ultrahigh-speed synchrotron X-ray imaging to capture the
90 keyhole evolution across a range of process conditions for a Ti6Al4V alloy.

91 The effect of the process parameters on the quality is indirect, namely through the melting
92 process. Therefore, it is important to understand the relation between the melting behaviour and
93 the part quality. It is known that the melt pool characteristics such as melt pool geometry and its
94 thermal distribution are an indicator of the final microstructure, which can strongly affect the
95 mechanical property of the final build part [16]. An in-process melt pool monitoring system is a
96 useful tool to inspect the melt pool behaviour during the LPBF process [17]. Along with the in-
97 situ observations, multi-physics simulations of the LPBF process are very helpful in
98 understanding the mechanisms of defect formation. These models enable the analysis of the melt
99 pool's thermo-fluidic behaviour with a very fine spatial-temporal resolution and involve various
100 physical phenomena, e.g. evaporation, solidification, capillarity, etc. Multi-physics models have
101 already been implemented by some of the co-authors to study the mechanisms of lack-of-fusion
102 and keyhole-induced porosities during the LPBF process [12]. These models are found to be very
103 accurate in determining the size, shape and the possible locations of the pores.

104 During the powder bed fusion process, spatter particles may eject from the melt pool due to
105 multi-physics phenomena. These spatter particles can have an impact on the part quality as large
106 spatter particles that land on the top of the powder layer may attenuate the laser beam, resulting
107 in lack of fusion porosity, and may increase surface roughness. Therefore, the identification and
108 analysis of spatter are considered important. Matthews et al., 2016 [18] observed the denudation
109 phenomena near the laser scan track using high-speed imaging and explained that for a typical
110 environment, inward gas flow driven by a metal vapour jet due to the Bernoulli effect was the
111 dominant driving force for denuding powder near a melt track. Ly et al., 2017 [19] explained the

112 physics of droplet ejection by ultra-high speed imaging of the melt pool. They presented detailed
113 experiments and finite element modelling of metal micro-droplets to explain the physics of the
114 laser-vapour-driven particle entrainment. Gunenthiram et al., 2018 [20] investigated metallic
115 ejections generated during SLM using a high speed camera. Image analysis was performed for
116 spatter analysis and a correlation was proposed between the volume of spatters and volume
117 energy densities (VED) to identify melt-pool stability regimes. Repossini et al., 2017 [21]
118 monitored spatter using an off-axis camera with a large field-of-view installed on their machine.
119 Basic image processing, like the simple thresholding method, was used to binarize the recorded
120 images. The binary images are then further processed to extract some features related to spatter,
121 like the number of spatters, the average spatter area and the speed of ejected spatters.

122 This paper focuses on melt pool and spatter analysis in LPBF builds for Ti-6Al-4V grade 23.
123 Both the melt pool characteristics (intensity, geometry) and spatter can be observed with the in-
124 process coaxial monitoring system. The current work presents a first attempt to characterize
125 spatter on coaxial camera images recorded from a coaxial monitoring system and to link it to the
126 keyhole pores' formation. An important challenge in analysing the coaxial camera images is that
127 in many cases the melt pool is overlapping with the spatters. In addition, in some cases, the
128 intensity of spatters in the images is quite low. Hence, applying a basic thresholding method to
129 the images will miss-detect spatters ejected from the melt pool. Therefore, a novel combination
130 of image processing steps are proposed in this paper to highlight and enhance both spatters
131 overlapping with the melt pool and spatters with low intensity. The paper is structured as
132 follows. Section 2 reviews the experimental procedure including the description of the
133 measurement set-up and the algorithmic flow to process the collected data and to transform them
134 into monitoring features. Furthermore, the measurements obtained through optical microscopy
135 and X-ray tomography, as well as melt pool CFD simulations are described. Section 3 discusses
136 the results at nominal and deviating volumetric energy density conditions obtained from
137 experimental and modelling analyses. Conclusions are formulated in Section 4.

138 **2. Experimental procedure**

139 **2.1 LPBF process**

140 An in-house developed LPBF machine of KU Leuven (LM-Q) was used to build the parts under
141 investigation. This machine is equipped with an Ytterbium (Yb) continuous wave fibre laser
142 source with a wavelength of 1080 nm and maximum output power of 1 kW. The focused laser
143 beam has a spot diameter of 37.5 μm (\emptyset_{1/e^2} : 13.5% of maximum). The subject of the
144 investigation presented here are single-line tracks, built on dense LPBF substrates (10 mm x 10
145 mm x 5 mm). The feedstock material used is Ti-6Al-4V grade 23 powder, with a powder particle
146 size ranging between 15 - 45 μm . The dense substrates are built using optimized process
147 parameters (see Table 1) that are, in their turn, optimized based on the maximum achieved
148 Archimedes' part density. The layer thickness is set at 30 μm , both for the substrates and the
149 single line tracks. The scan strategy for the substrate is contour first, with a bi-directional infill
150 and a rotation of 90 degrees between layers. The single tracks are produced simultaneously with
151 the substrates, in a single job, to mimic normal processing conditions. For the single line tracks,
152 the Volumetric Energy Density (VED) is modified by adapting both the scan speed and the laser
153 power. The applied VEDs are subdivided into three regions, identified as being low, optimum
154 and high VED (Table 1). The VED in Table 1 is calculated by using the following equation:

$$VED = \frac{P}{v \cdot d \cdot t} \quad (1)$$

155 where VED is the applied volumetric energy density (J/mm^3), P is the laser power (W), v is the
 156 scan speed (mm/s), t is the layer thickness (mm) and d is the spot diameter (mm).

157 **Table 1.** Process parameter for LPBF of Ti-6Al-4V.

Condition	ID	Laser Power / W	Scan Speed / $\text{mm} \cdot \text{s}^{-1}$	Volumetric energy density (VED) / $\text{J} \cdot \text{mm}^{-3}$
Optimum VED	1	170	1000	151.11
High VED	2	340	1000	302.22
	3	170	500	
Low VED	4	85	1000	75.55
	5	170	2000	

158 In previous work [22], in which the same samples were examined, it was shown that for an
 159 identical high VED¹ (i.e. ID# 2 and 3), a lower scan speed at the optimum laser power resulted in
 160 keyhole porosities, while a higher laser power at the optimum scan speed did not have the same
 161 detrimental effect. This study focuses on the analysis of the experimental condition leading to
 162 keyhole porosities (ID# 3 in Table 1). A comparison (both experimentally and through
 163 modelling) is thus made with the condition under optimum process parameters (ID# 1 in Table 1)
 164 and the condition at high VED (ID# 3 in Table 1).

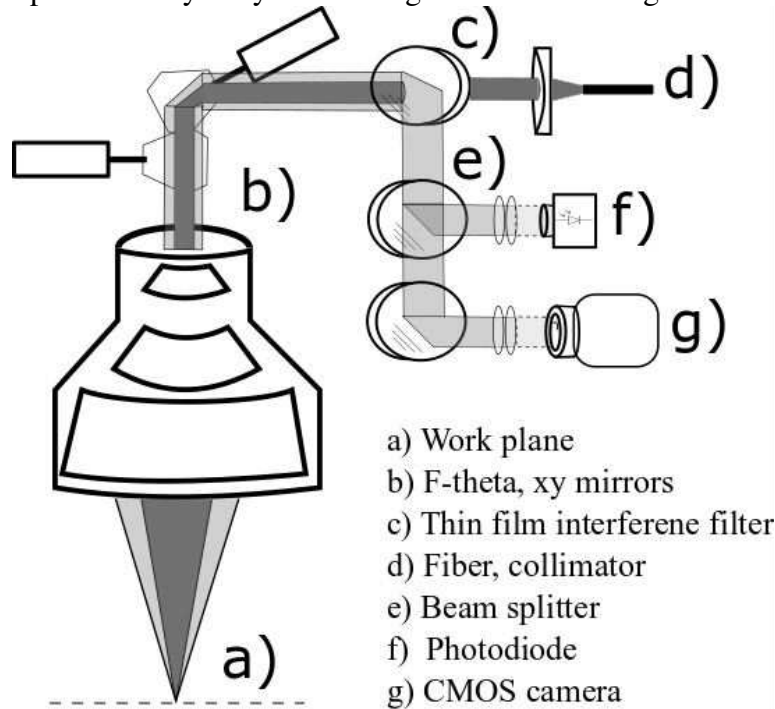
165 Extracting melt pool dimensions using metallographic analysis is challenging for Ti-6Al-4V, as
 166 the melt pool boundaries are not readily revealed by etching. Alternatively, the melt pool width
 167 is measured by imaging the top surface, by means of a Keyence VHX-600 optical microscope.
 168 The depth dimension is estimated by examining the keyhole porosity depth using X-CT cross-
 169 sections.

170 **2.2 In-process melt pool monitoring**

171 The in-house developed LPBF machine of KU Leuven (LM-Q) is equipped with a coaxial melt
 172 pool monitoring set-up. A description of the conceptual operation and components is given in
 173 this section. The general layout is schematically shown in Figure 2. The laser source of 1080 nm
 174 wavelength is collimated (d), coupled into free space, and guided through an optic with a thin-
 175 film interference filter (c). The filter is designed to have a cut-on wavelength of 950 nm i.e.

¹ In [22] the laser spot diameter was assumed to be 50 μm , resulting in slightly smaller reported VED values as compared to the values reported here. Afterwards the laser spot size was measured to be 37,5 μm leading to the corrected VED values shown in Table 1.

176 wavelengths above 950 nm are transmitted, while those below the cut-on wavelength are
 177 reflected. This filter is thus allowing the laser beam to pass freely through the optic. After the
 178 filter, the laser is positioned and focused on the powder bed using a Galvano-scanner and f-theta
 179 lens combination (b). When the laser hits the powder at the workplace (a), a melt pool is created
 180 and according to the black-body radiation theory (Planck's law), a spectrum of radiation is
 181 emitted depending on the object temperature. Part of the generated melt pool radiation or process
 182 light is transmitted back into the f-theta lens and Galvano-scanner combination (b). The process
 183 light is then separated from the laser source by reflecting off the thin-film interference filter (c).
 184 After separation, the process light is distributed evenly among the two sensors using a beam
 185 splitter (e). The two sensors are a silicon photodiode (f) [23] and a CMOS camera (g) [24]. Both
 186 the sensors are band-passed filtered to have the near-infrared (NIR) wavelength range between
 187 800-950 nm for observation of the melt pool radiation. Filtering eliminates any remaining laser
 188 emission, as well as prohibits any stray ambient light from interfering with the measurements.



189

190 **Figure 2.** Schematic overview of the monitoring setup.

191 The analogue signal originating from the photodiode (f) is sampled using a sample and hold
 192 analogue-to-digital converter with 16-bit resolution (-10, 10 V) with the sampling frequency of
 193 20 kHz. The photodiode signal is synchronized and simultaneously logged together with the
 194 scanner XY-positions.

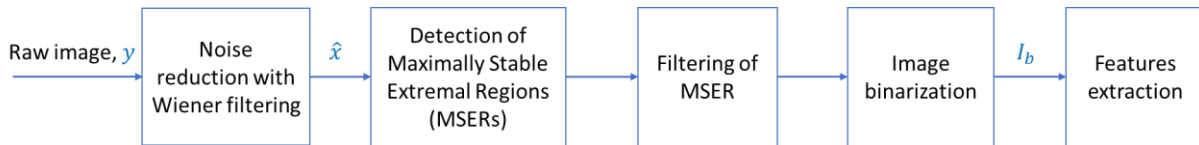
195 The CMOS camera (g) is connected to a separate frame grabber system, using the Camera Link®
 196 interface. The images measure 80 by 80 pixels and have an 8-bit grayscale pixel depth. The pixel
 197 size is measured to be 14 μm by employing an R3L3S3P concentric square target calibration
 198 plate manufactured by Thorlabs and is placed in the working plane. This results in a field of view
 199 of 1120 μm by 1120 μm. Thus, both the melt pool and surrounding environment are captured by
 200 the images, allowing for the occasional spatter to be captured by the camera. An example image

201 during operation is shown in Figure 4, showing both the melt pool and some spatter particles
 202 being ejected from said melt pool. The grayscale image intensities are inverted for clarity
 203 (0=white, 255=black).

204 The acquisition frame rate is fixed at 20,000 fps (frames per second). The camera acquisition is
 205 triggered with the machine controller’s data logging signal, synchronizing photodiode, scanner
 206 coordinates and camera images. All images are transferred and stored to a parallel RAID 0 SSD
 207 array containing 6 disks, capable of sustaining a data rate exceeding 1 GB/s. This assures that the
 208 maximum supported Camera Link® data rate of 850 MB/s is achievable throughout the entire
 209 process.

210 **2.3 Image processing steps for extracting geometrical and spatter features from the**
 211 **camera melt pool images**

212 Figure 3 shows the flowchart of the image processing and features extraction steps for
 213 characterising the melt pool geometry and spatters applied to the coaxial camera image. The
 214 innovation proposed in this paper is a combination of different existing image processing
 215 algorithms that are used in a particular sequence. The algorithms have been implemented in a
 216 MATLAB environment. In the first step, the noise that might be originating from the imaging
 217 sensor and/or the optical path in a raw image is suppressed by applying a Wiener filtering
 218 technique [25]. In the second step, the denoised image is further processed by identifying and
 219 localizing several co-variant regions called Maximally Stable Extremal Regions (MSERs) in the
 220 image [26]. In the third step, a filter is applied to select a representative MSER from the detected
 221 co-located MSERs. In the fourth step, a binary image is generated by setting the selected regions
 222 in the image to one and keeping the other regions to zero. In the final step, some geometrical and
 223 spatter-related features are extracted from the binarized image. Each step is briefly explained in
 224 the forthcoming subsections.



225 **Figure 3.** Flowchart of the image processing algorithm for spatter detection.

226 **2.3.1 Wiener filtering for image denoising**

227 Suppose that a measured image is corrupted by independent zero-mean white Gaussian noise.
 228 The problem can be formulated as follows:

$$y(n, m) = h(n, m) * x(n, m) + v(n, m) \tag{2}$$

229 Where $y(n, m)$ denotes the measured image with n and m being the pixel indices, $h(n, m)$
 230 denoting the linear time-invariant impulse response function of the optical path, $x(n, m)$ is the
 231 (unknown) true image, the operator $*$ denoting convolution and $v(n, m)$ denoting the
 232 measurement noise.

233 The objective is to remove noise or denoise $y(n, m)$ and to obtain an estimate $\hat{x}(n, m)$ of
 234 $x(n, m)$, which minimizes the mean squared error (MSE),

$$MSE(\hat{\mathbf{x}}) = \frac{1}{N} \sum_{n,m=1}^N (\hat{x}(n, m) - x(n, m))^2 \quad (3)$$

235 where N denotes the number of pixel elements in $x(n, m)$.

236 When $x(n, m)$ and $v(n, m)$ are stationary Gaussian processes, the Wiener filter is the optimal
 237 filter [25]. Specifically, when $x(n, m)$ is also a white Gaussian process, the Wiener filter can be
 238 simply formulated as follows:

$$\hat{x}(n, m) = \mu_x(n, m) + \frac{\sigma_x^2(n, m)}{\sigma_x^2(n, m) + \sigma_n^2(n, m)} [y(n, m) - \mu_x(n, m)] \quad (4)$$

239 Where σ^2 and μ are the image variances and means, respectively. To use Eq. (4), the image
 240 mean $\mu_x(n, m)$, the image variance $\sigma_x^2(n, m)$ and the noise variance $\sigma_n^2(n, m)$ need to be
 241 determined. If the noise variance is unknown, it is taken equal to the average of all the local
 242 estimated variances. The image mean and variance are calculated locally around each pixel over
 243 a uniform moving average window of size $(2r + 1) \times (2r + 1)$:

$$\hat{\mu}_x(n, m) = \frac{1}{(2r + 1)^2} \left[\sum_{p=n-r}^{n+r} \sum_{q=m-r}^{m+r} y(p, q) \right] \quad (5)$$

$$\hat{\sigma}_x^2(n, m) = \frac{1}{(2r + 1)^2} \left[\sum_{p=n-r}^{n+r} \sum_{q=m-r}^{m+r} (y(p, q) - \hat{\mu}_x(n, m))^2 - \sigma_n^2(n, m) \right] \quad (6)$$

244 With the parameter r denoting an integer value. The choice of the parameter r for determining
 245 the window size for averaging depends on the image size. Moreover, the choice is application-
 246 specific and should be determined experimentally. However, according to [26], the value of the
 247 parameter r should be selected around 2 or 3.

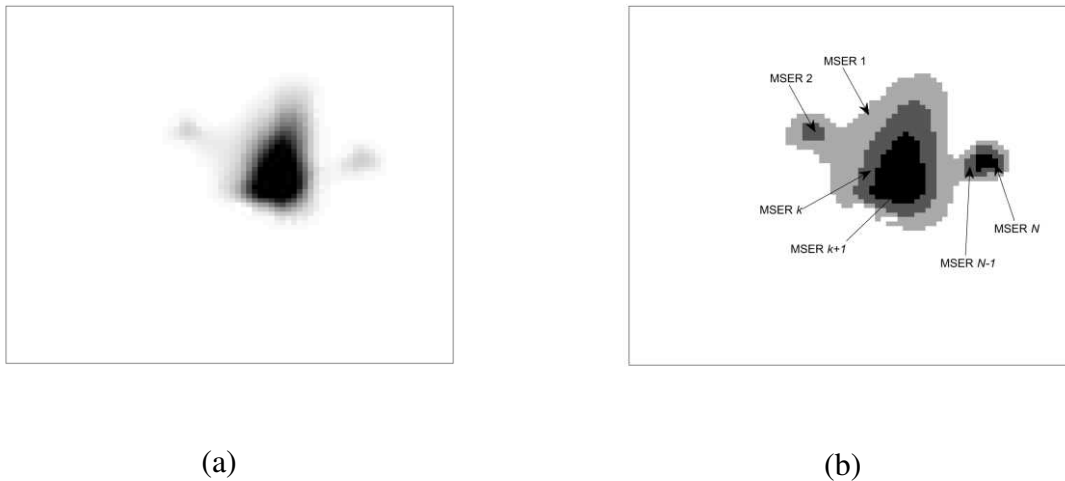
248 **2.3.2 Detection of Maximally Stable Extremal Regions (MSERs)**

249 Maximally Stable Extremal Regions (MSERs) are connected areas characterised by almost
 250 uniform intensity, surrounded by contrasting backgrounds. MSERs are constructed through a
 251 process of trying multiple thresholds. The selected regions are those that maintain unchanged
 252 shapes over a large set of thresholds [27]. The concept of MSER can be explained as follows.
 253 Assume that there exist all possible thresholds of a grey-level image $I = \hat{x}$. Define pixels below
 254 a threshold as 'white' and those above or equal to the threshold as 'black'. If thresholded images
 255 I_t are shown one after the other, with time frame t being also the threshold t , a black image will
 256 first appear at $t=0$. Subsequently, white spots corresponding to local intensity minima will appear
 257 and grow. At some point, regions corresponding to local minima will merge, enclosing black
 258 regions of high value pixels. For increasing threshold, these black regions will shrink. Finally,

259 the last image will be completely white. The set of all connected components of all frames of the
260 movie is the set of all maximal regions (MSER 1, MSER 2, ..., MSER k , ..., MSER N), as seen in
261 Figure 4 (b). The reader is referred to [27] for a more thorough description of the method.

262 2.3.3 Filtering

263 In case where some MSERs are co-located, for example, MSER k with MSER $k + 1$, and
264 MSER $N - 1$ with MSER N as illustrated in Figure 4 (b), filtering needs to be applied to select
265 the most representative MSER. The first step is to check whether co-located MSERs exist. To
266 this end, an MSER with the largest area is selected as a reference MSER. Then, the distance
267 between the centroid of a benchmarked MSER and that of the reference MSER is calculated. If
268 the centroid distance is smaller than a certain threshold, the benchmarked MSER is thus co-
269 located with the reference MSER. The second-largest area of the co-located MSERs is selected
270 as a representative MSER. Based on the illustrative example shown in Figure 4 (b), the
271 representative MSER for the two co-located MSER k and MSER $k + 1$ is MSER k , while the
272 representative one for the two co-located MSER $N - 1$ and MSER N is MSER $N - 1$.



273 **Figure 4.** An illustrative example of identification of MSERs from an image: (a) raw/pre-
274 processed image, (b) MSERs identified from the image.

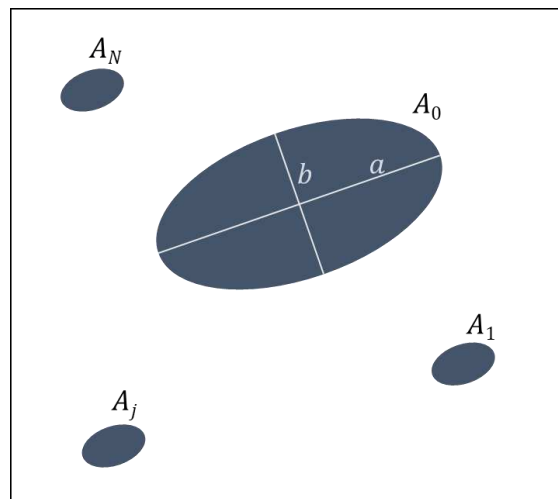
275 2.3.4 Image binarization

276 Once co-located and non-co-located MSERs are selected, the binary image I_b is simply
277 generated by setting the pixel values on the selected MSERs to one (black), and by setting the
278 pixel values of the background to zero (white).

279 2.3.5 Features calculation

280 Figure 5 illustrates several features that are extracted from the binary image I_b . The largest
281 object detected in the binary image A_0 is taken as the melt pool, while the smaller objects
282 ($A_1, \dots, A_j, \dots, A_N$) are taken as spatters. The first defined features are the length, width and area.
283 They are extracted using Hu's Moment Invariants [28] as implemented in the MATLAB

284 environment. The area is calculated by taking the 0th moment, which is the equivalent to the total
 285 number of pixels of the original object. To determine the length and width, an ellipse that has the
 286 same normalized second central moments as the segmented object is construed for each object,
 287 as can be seen in Figure 5. The size of the principal axes of the equivalent ellipses then represent
 288 the length and width (major axis (a) and minor axis (b) respectively). The second feature is the
 289 main melt pool eccentricity, $\varepsilon = \sqrt{1 - \frac{b^2}{a^2}}$, $b < a$. The third feature is the perimeter of the main
 290 melt pool ρ . The fourth feature is the number of spatter, N . The fifth feature is the spatter ratio r
 291 being defined as the division between the total area of spatters and the main melt pool area,
 292 $r = \frac{\sum_{j=1}^N A_j}{A_0}$. The first 3 features are expressed as scalars in the unit of pixel. The remaining 2,
 293 number of spatter and spatter ratio, are dimensionless.



294 **Figure 5.** Illustration of features calculated from a binary image I_b .

295 **2.4 X-ray computed tomography**

296 X-ray computed tomography (X-CT) measurements are performed to scan the object with a XT
 297 H 225 ST machine from Nikon Metrology having a maximum tube potential of 225 kV. The
 298 instrumental parameters are set at a tube voltage of 180 kV, a power of 12.1 W, an exposure time
 299 of 2000 ms and 3600 radiographs. The chosen target material for the X-ray generation is
 300 tungsten. The magnification is fixed at a factor of 20, prompting a measurement resolution
 301 (voxel size) of 10 μm . A copper filter of 1 mm thickness is utilized in front of the X-ray tube
 302 window to reduce the beam hardening effect. The volume reconstruction is performed using the
 303 Feldkamp-Davis-Kress algorithm. The alignment of the reconstructed volume is performed by
 304 the 3-2-1 registration technique with VGStudio MAX 3.2 software.

305 **2.5 Numerical modelling of the melt pool**

306 A Finite Volume Method based Computational Fluid Dynamics (CFD) model introduced by
 307 Bayat et al., 2019 [12] is used to simulate the heat and fluid flow conditions for both optimum
 308 and keyhole LPBF conditions. The model solves the conservation of mass, linear momentum and
 309 energy equations. It uses the Fresnel absorption function to model the laser behaviour [29],

310 which is dependent on the geometry of the depression zone. The model also takes into account
311 several physical based phenomena such as evaporation, ablation pressure, melting, capillarity,
312 Marangoni effect, solidification and the laser-material interaction [30]. Besides, it encompasses
313 the ambient heat losses through the exposed free surfaces via convection, radiation and
314 evaporation.

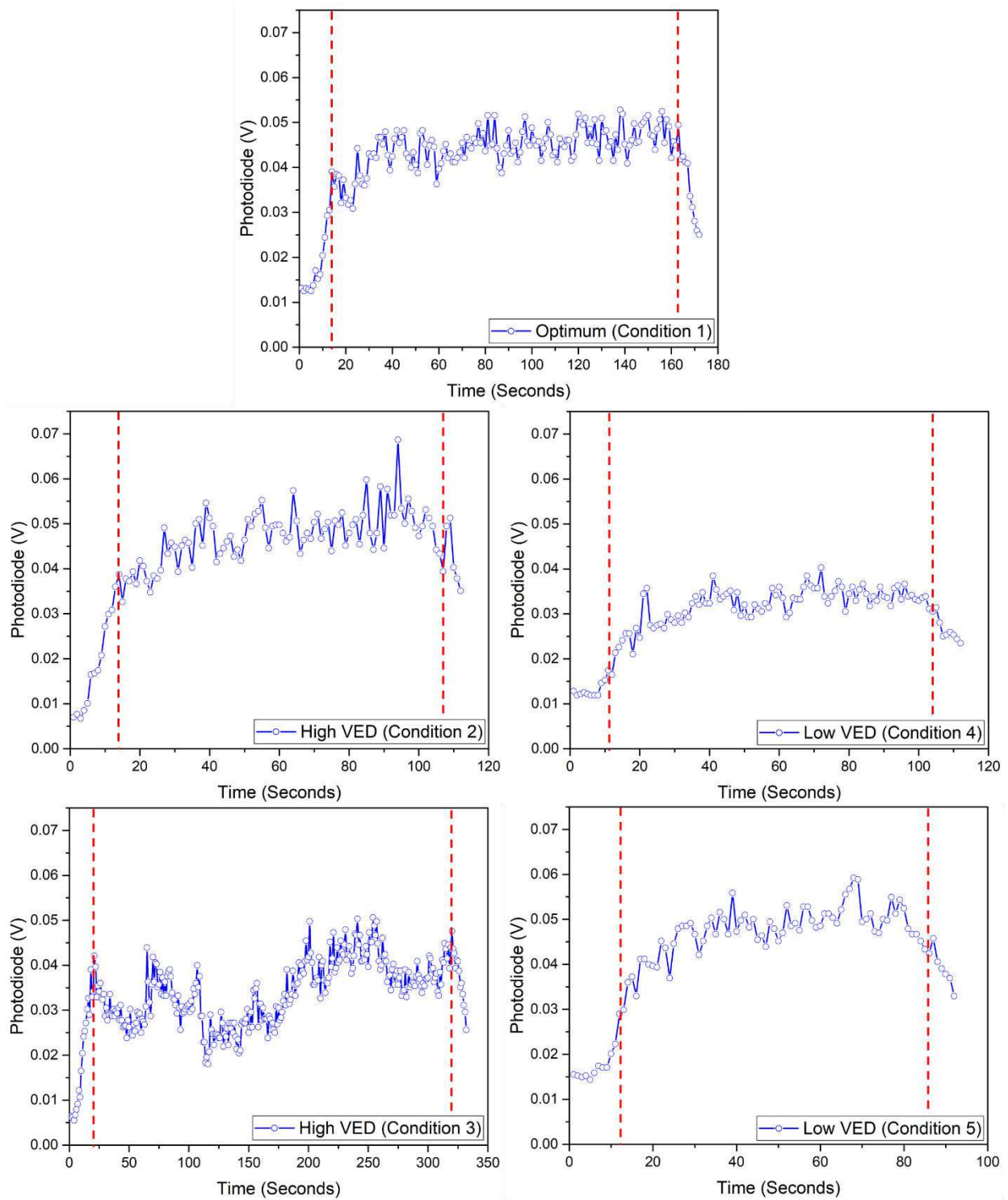
315 **3. Results and discussion**

316 The first part of this section shows the geometrical features of a melt pool comprising of the
317 major axis-length, the minor axis-width and the melt pool area, as measured from the coaxial
318 camera melt pool images of the single track experiment. The second part discusses the features
319 comprising the number of spatters, the spatter area and the spatter ratio of the single track
320 experiment. The third part presents numerical modelling results of the melt pool for optimum
321 and keyhole LPBF conditions. In the final part of this section, melt pool geometry features are
322 evaluated from optical micrographs.

323 **3.1 Geometrical melt pool features for the single track experiment**

324 This section shows the results from the photodiode and the high-speed camera for single tracks.
325 The photodiode indicates the average melt pool intensity (single value output) and the high-
326 speed coaxial camera records the melt pool geometry (2D array of pixels) from which melt pool
327 characteristics like length and width are extracted. Table 2 shows the melt pool intensity for line
328 scans with different processing parameters. The average intensity of six line-scans is presented
329 with its associated standard deviation. The first up to 15 data points in the beginning and up to 10
330 data points at the end of the line scan are neglected due to the non-uniformity of the applied
331 energy density. This is a result of the acceleration and deceleration of the galvanometer mirrors.
332 The melt pool emission energy is calculated by averaging the photodiode signal and
333 subsequently integrating over time, for a certain line length e.g. 1000 mm. This integrated value
334 logically increases with decreasing scan speed (longer duration) if the average emitted intensity
335 remains the same.

336 However, it is clear from Table 2 that the average melt pool emission intensity does not scale
337 linearly with the volumetric energy density (VED). Indeed, it is found that the recorded average
338 signal from the photodiode for condition 2 is 14.7% higher than for optimum condition 1. While
339 for condition 3 the recorded average signal is 13.2% lower than what was found for condition 1,
340 even though both are observed to have the same VED. Alternatively, examining the average
341 integrated melt pool intensity, condition 3 now exhibits the highest value. For condition 3 the
342 integrated average value is 73.5% higher compared to condition 1. In contrast, condition 2
343 exhibits the same 14.7% increase in integrated average value compared to optimum condition 1.
344 These results could indicate that the occurrence of keyhole mode melting (condition 3) is tied
345 with the integrated average of the melt pool radiation, while simultaneously it is less dependent
346 on the average measured radiation. Figure 6 shows examples of the recorded melt pool intensity
347 for a single track with optimum, high and low VED conditions.



348

349 **Figure 6.** Melt pool intensity (photodiode signal (V)) of single track with optimum, high and low
 350 VED conditions. Data between two dashed red lines are taken into account.

351

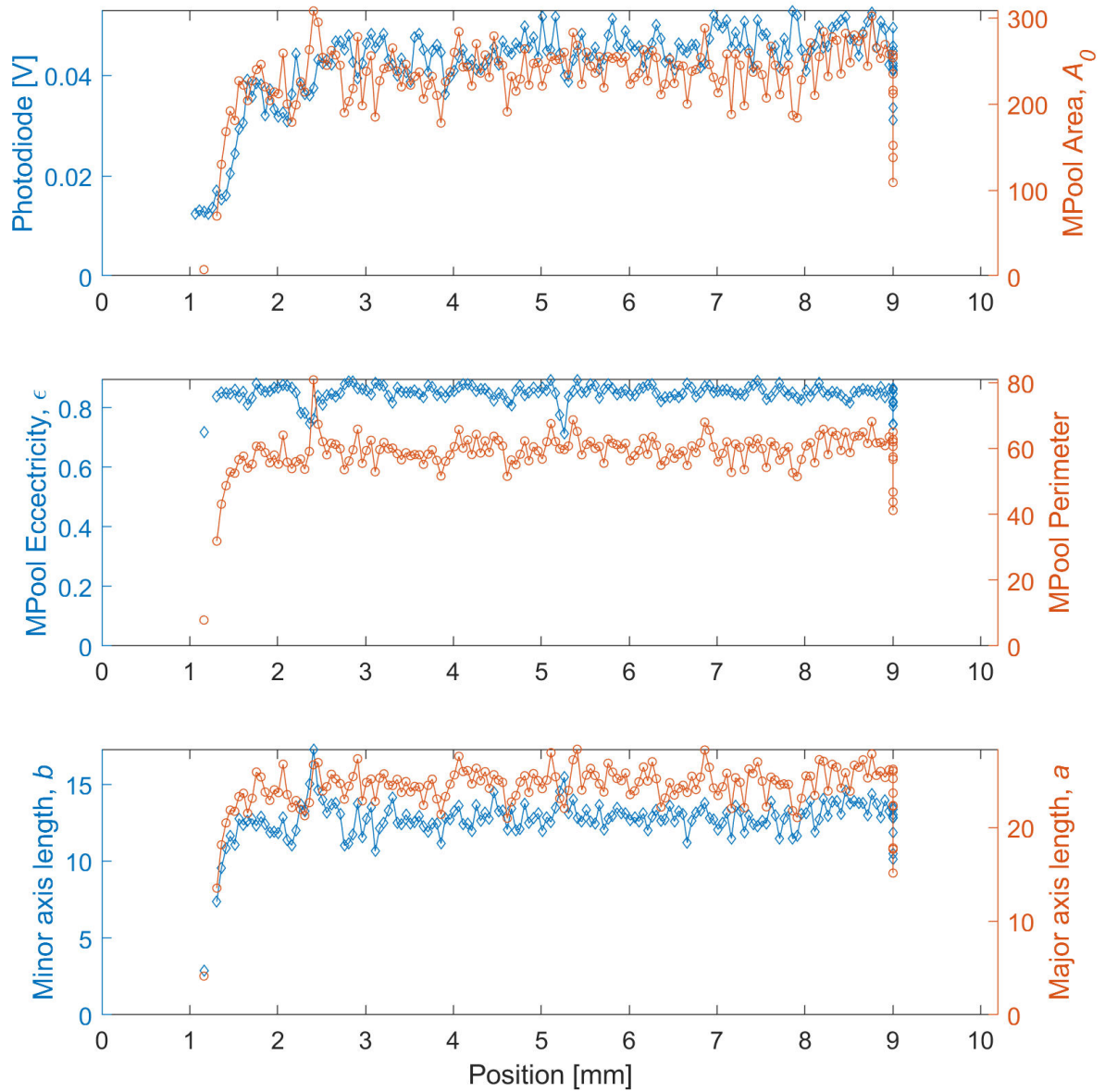
352

Table 2. Melt pool (MP) Intensity from Photodiode for LPBF of Ti-6Al-4V.

Condition and VED	ID	Laser Power / W	Scan Speed / $\text{mm}\cdot\text{s}^{-1}$	Average MP Intensity / mV	Integrated intensity over time for a length of 1000 mm / $\text{V}\cdot\text{s}$
Optimum VED ($151 \text{ J}\cdot\text{mm}^{-3}$)	1	170	1000	40.1 ± 1.5	0.0401
High VED ($302 \text{ J}\cdot\text{mm}^{-3}$)	2	340	1000	46.0 ± 1.7	0.0460
	3	170	500	34.9 ± 0.7	0.0696
Low VED ($75.6 \text{ J}\cdot\text{mm}^{-3}$)	4	85	1000	29.7 ± 1.9	0.0297
	5	170	2000	43.4 ± 1.7	0.0216

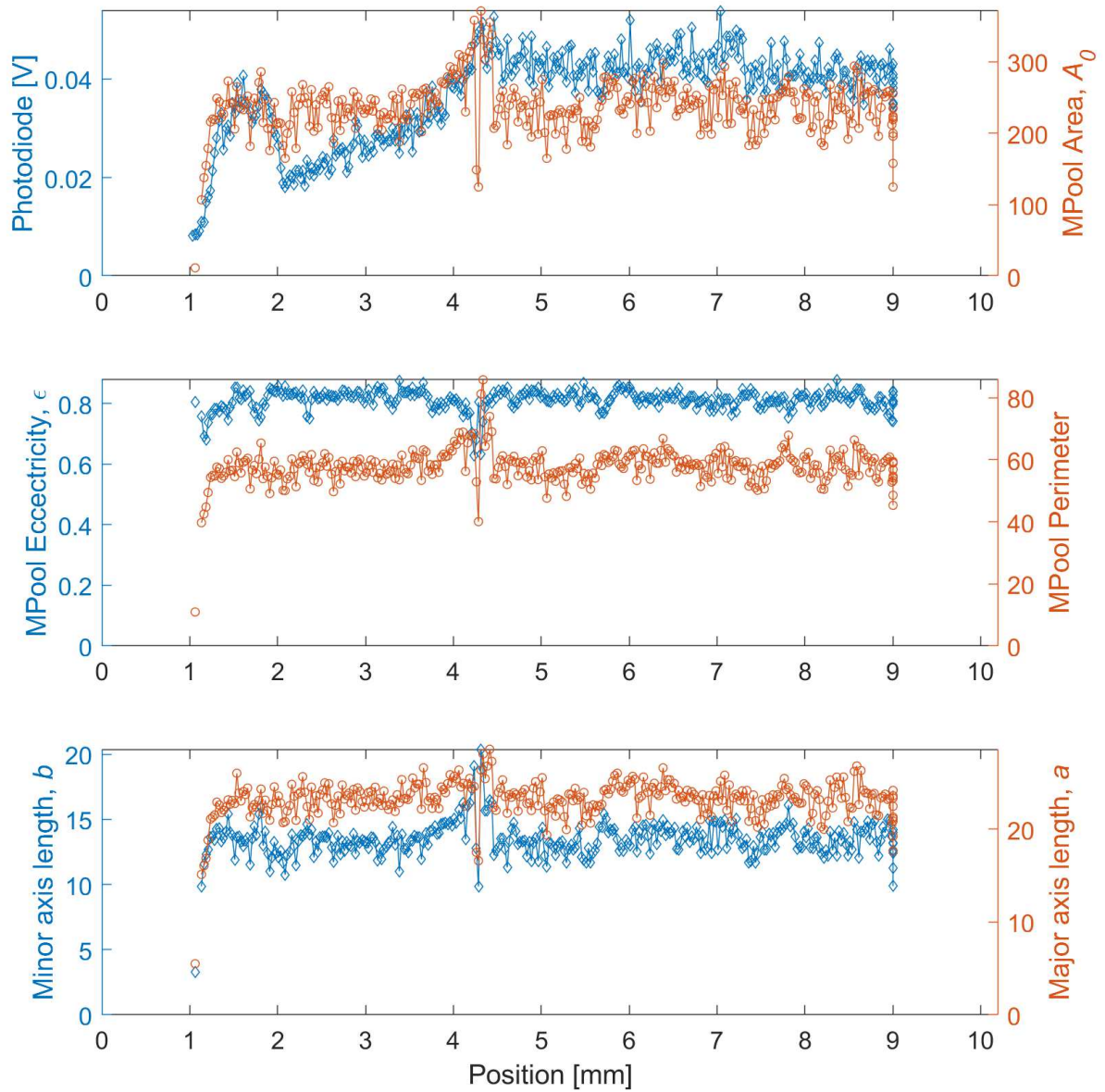
354 In order to extract the melt pool geometry from the grayscale camera images, the camera images
355 are pre-processed using the processing steps detailed in Section 2.3 to generate binary images.
356 Some geometrical features including the melt pool length, width and area are calculated in units
357 of pixels. For the single track experiments, the pixel size is equal to roughly $14 \mu\text{m}$ after camera
358 calibration. Figure 7 shows the different melt pool features for an optimum condition (condition
359 1, $P = 170 \text{ W}$, $v = 1000 \text{ mm}\cdot\text{s}^{-1}$) and Figure 8 shows the different melt pool features for a high
360 VED (condition 3, $P = 170 \text{ W}$, $v = 500 \text{ mm}\cdot\text{s}^{-1}$). The average melt pool geometry results of all six
361 line scans with optimum and keyhole conditions are presented in Table 3. As can be seen from
362 the recorded and average melt pool dimensions, no significant difference in the melt pool area,
363 width and length for the optimum (condition 1) and the keyhole mode (condition 3) is observed.
364 While the average melt pool length is shorter and the width is larger for condition 3 as compared
365 to condition 1, the variations are larger than the difference in dimensions, making the difference
366 statistically insignificant.

367 Figure 7 shows a very stable melt pool during the optimum process parameters (condition 1). In
368 Figure 8 however, an unstable melt pool, as well as melt pool anomalies, are observed during the
369 line scan for condition 3. These anomalies are due to spatter ejecting from the melt pool during
370 processing. Indeed, a peak in the melt pool area and perimeter does not necessarily mean that the
371 melt pool grows to be very large. Instead due to the 2D representation of a 3D space, both the
372 spatter and the melt pool appear to be connected resulting in a large apparent area. In reality, the
373 spatter is situated in a plane above that of the melt pool. As soon as the spatter detaches from the
374 melt pool in the camera image, the melt pool area immediately drops back to the expected level
375 (for an illustration see last three pictures in Figure 13). In the next section, results from the image
376 processing algorithm for spatter detection are explained in detail after discussing possible spatter
377 formation mechanisms.



378

379 **Figure 7.** Melt pool features for the optimum condition (condition 1, $P = 170$ W, $v = 1000$ mm.s⁻¹).
 380



381

382 **Figure 8.** Melt pool features for a high VED (condition 3, $P = 170 \text{ W}$, $v = 500 \text{ mm.s}^{-1}$).

383

384

385

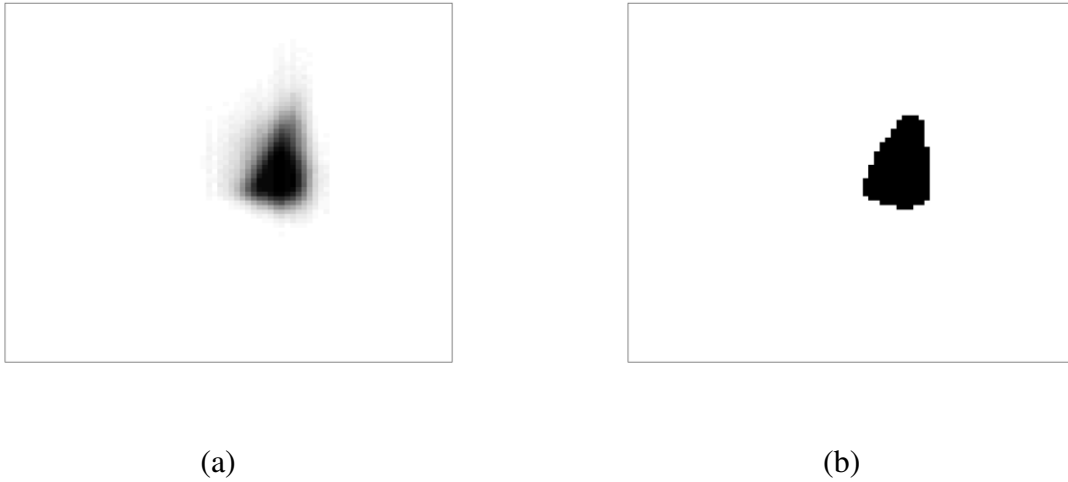
386 **Table 3.** The statistics of the melt pool geometrical features of optimum and keyhole conditions
 387 for LPBF of Ti-6Al-4V calculated from the position of 2 mm to 8 mm as shown in Figure 7 and
 388 8.

Condition	ID	Melt pool width / pixel	Melt pool length / pixel	Area / pixel ²	Perimeter / pixel	Eccentricity /
Optimum VED	1	12.8 ± 0.9	24.6 ± 1.6	237 ± 25	59 ± 4	0.85 ± 0.03
High VED	3	13.6 ± 1.3	23.5 ± 1.6	241 ± 34	58 ± 5	0.81 ± 0.03

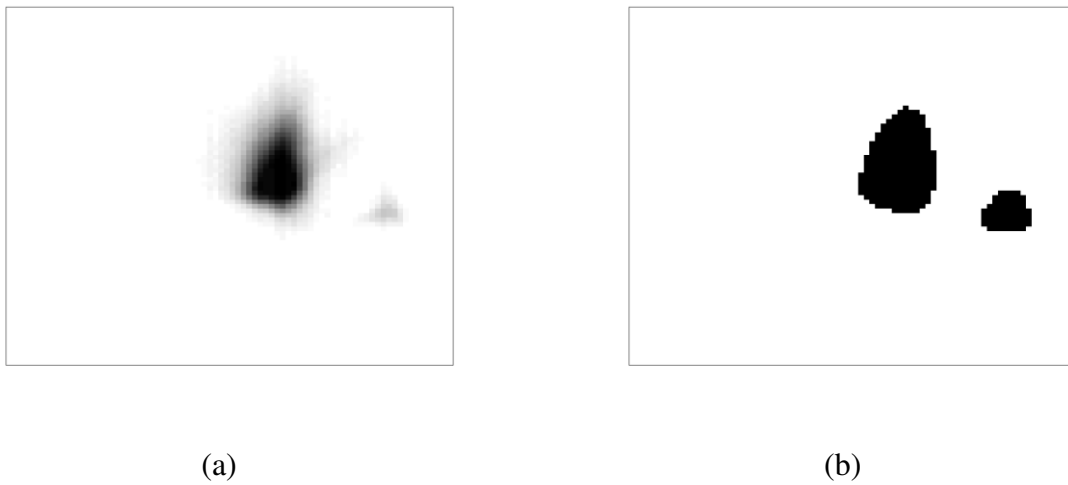
389 **3.2 Spatter features for the single track experiment**

390 The formation of spatter is a well-studied subject. Nevertheless, the correlation between the
 391 keyhole pore generation and the spatter formation observed in coaxial images remains unclear. A
 392 recent study by Young et al., 2020 [31], utilizing high speed x-ray imaging, distinguishes 5 types
 393 of spatters. Of these 5 types, only 2 are directly related to melt pool instabilities. Furthermore,
 394 they show that some types of spatters are always present irrespective of the processing conditions
 395 or melting mode. Wang et al., 2017 [32] distinguishes three types of spattering, mainly caused by
 396 melt pool instabilities due to Marangoni effect, recoil pressure and heat effect in molten pool. In
 397 general, two mechanisms of spatter formation are observed during keyhole mode melting. The
 398 first is related to the melt pool collapse as discussed before. The sudden breakdown of the
 399 keyhole is accompanied with a large change in the melt velocity and part of this melt can be
 400 pinched off during the collapse. This liquid metal stream elongates and breaks up into smaller
 401 droplets to minimize surface energy [9]. The second mechanism relates to the metallic jet stream
 402 coming from the keyhole because of the recoil pressure. The metallic vapour (typically ejected
 403 towards the rear) generates shear forces on the rear keyhole wall. These forces can reach such
 404 high levels that they can overcome the surface tension. As a result, liquid detachment can occur
 405 in the rear of the melt pool, generating spatter. Gunenthiram et al., 2018 [20] investigated and
 406 quantified the formation of spatters during an LPBF process and addressed the possible influence
 407 of keyhole formation on such instabilities. A correlation was proposed between volumes of
 408 spatters and volumetric energy density (VED). Repossini et al., 2017 [21] also showed that the
 409 over-melting condition produce a larger number of spatters than the nominal melting condition.
 410 In the analysis done in this work, we will investigate spatter formation for conditions 2 and 3 that
 411 have identical high VED.

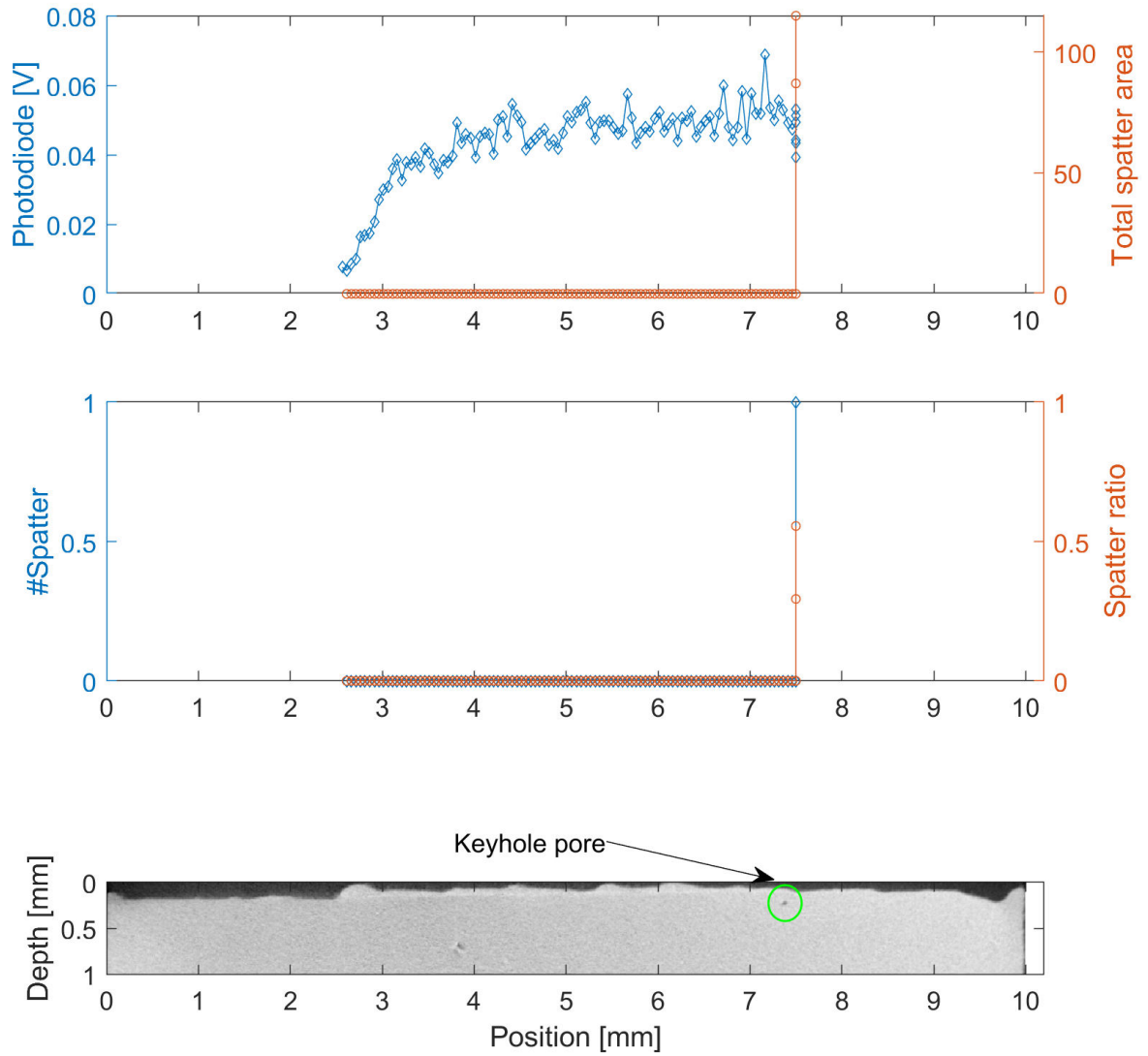
412 By employing a novel spatter detection workflow on high-speed coaxial images, a correlation
 413 can be made between the post-process X-CT observed keyhole porosity and the detected spatter
 414 in the images. Figure 9 and 10 show representative examples of the raw and processed coaxial
 415 melt pool images both in the absence and presence of spatters. The presence of spatters is not so
 416 obvious in the raw image, as shown in Figure 10 (a). Nevertheless, the spatters in the latter figure
 417 are effectively enhanced by the proposed algorithm, see Figure 10 (b).



418 **Figure 9.** An example of a processed image in the absence of spatters: (a) a raw image acquired
 419 by the melt pool monitoring system, (b) the binary image obtained by applying the image
 420 processing algorithm to the raw image.



421 **Figure 10.** An example of a processed image in the presence of spatters: (a) raw image acquired
 422 by the melt pool monitoring system, (b) the binary image obtained by applying the image
 423 processing algorithm to the raw image.

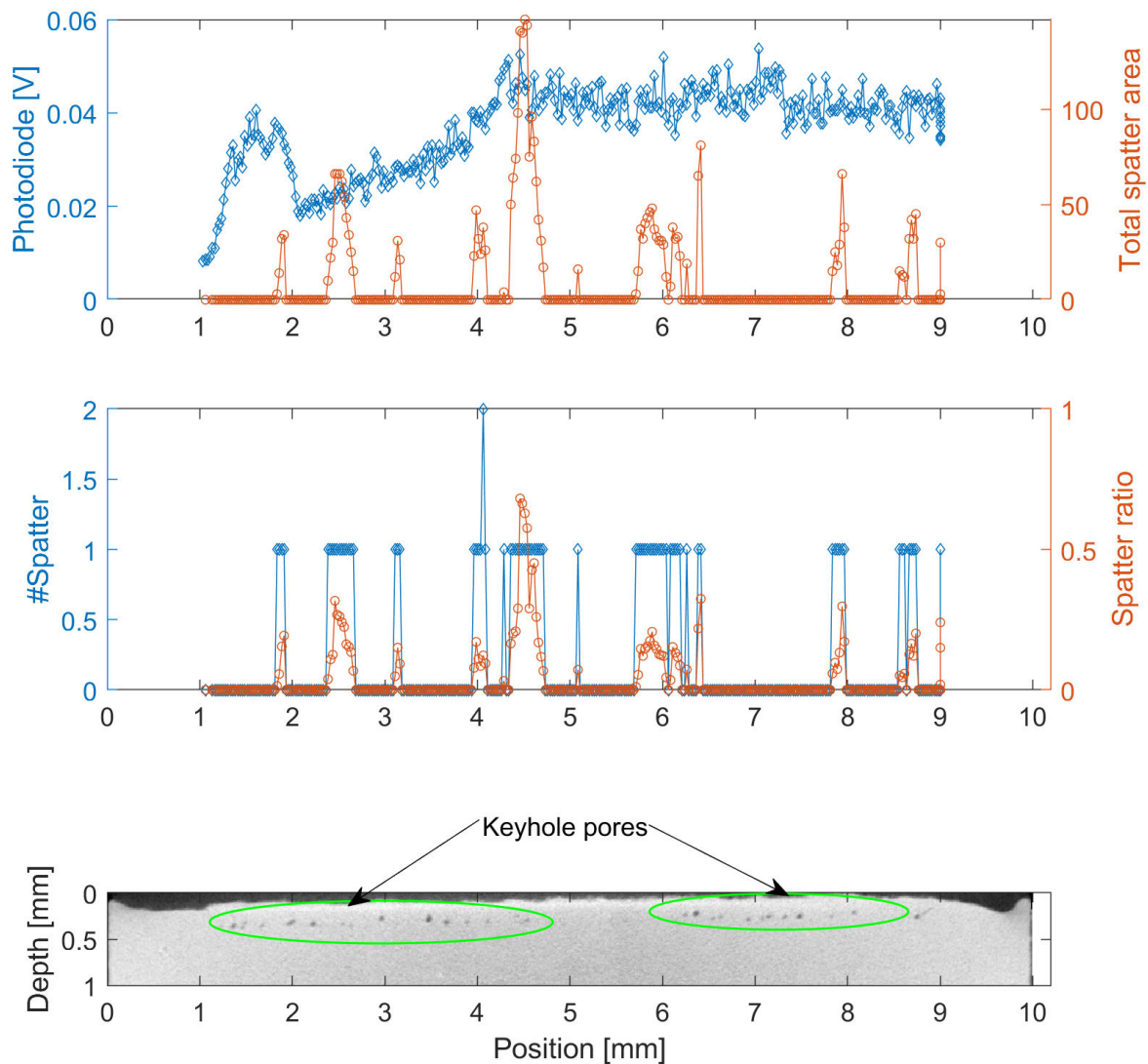


424

425

426

Figure 11. Comparison of spatter data calculated from melt pool images and porosity information obtained from X-CT for high VED (condition 2, $P = 340 \text{ W}$, $v = 1000 \text{ mm}\cdot\text{s}^{-1}$).

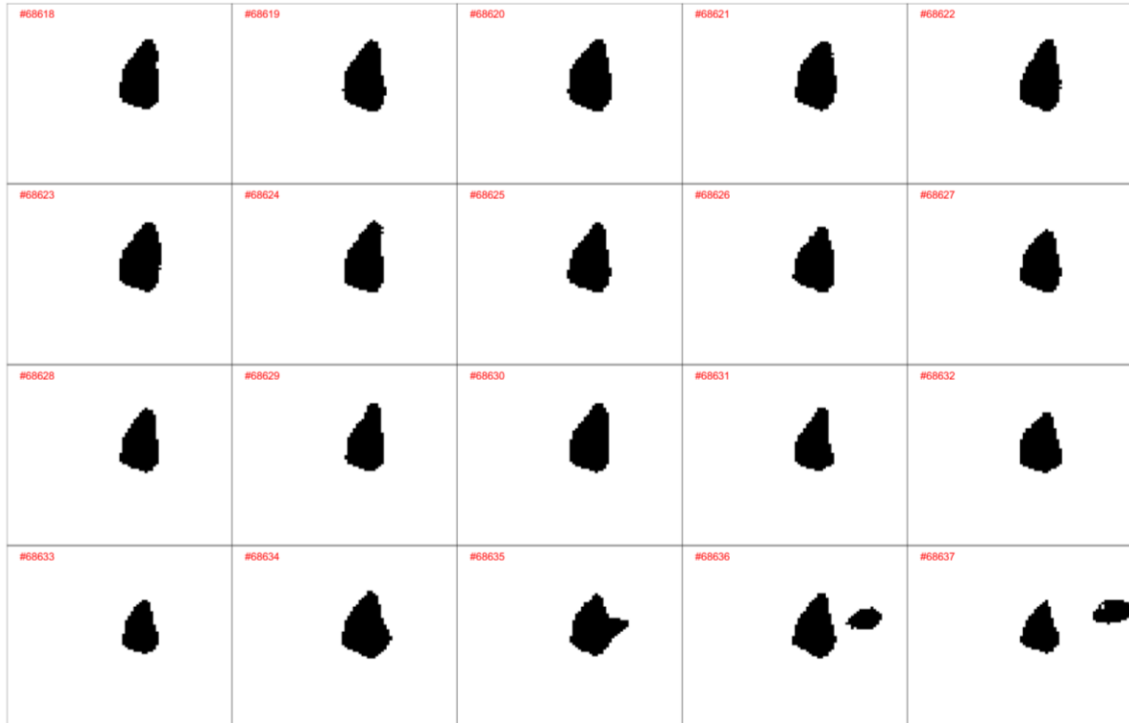


427

428 **Figure 12.** Comparison of spatter data calculated from melt pool images and porosity
 429 information obtained from X-CT for high VED (condition 3, $P = 170 \text{ W}$, $v = 500 \text{ mm}\cdot\text{s}^{-1}$).

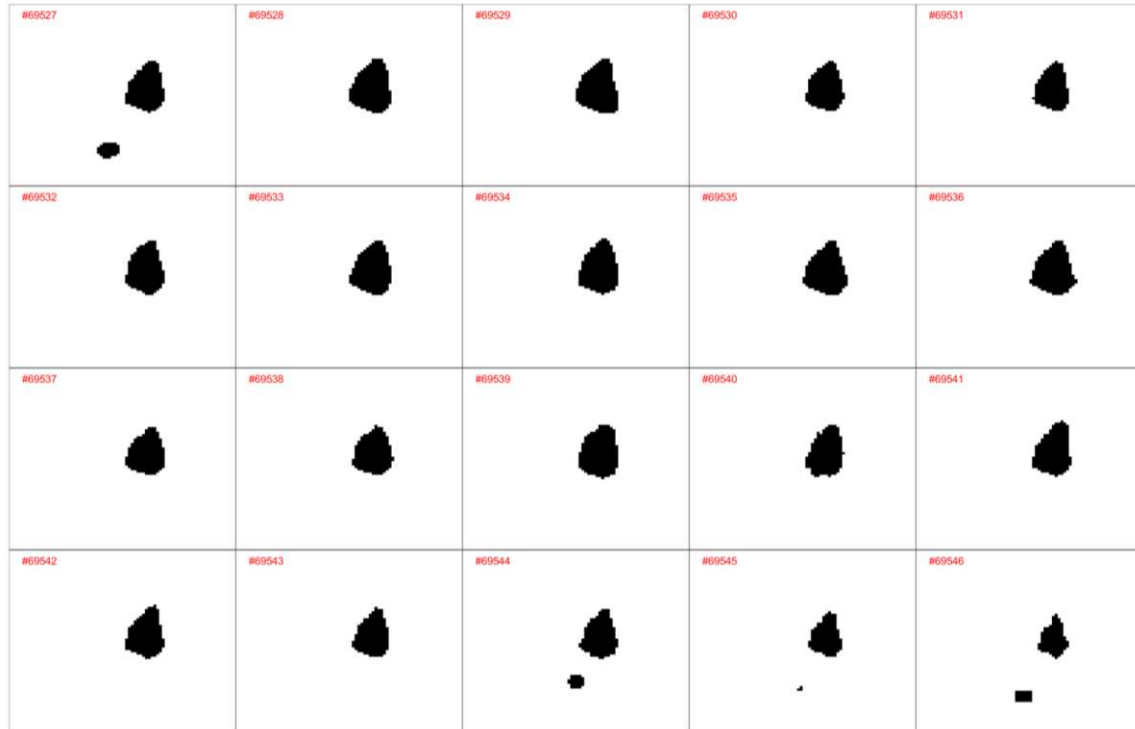
430 Figure 11 and 12 show the number of spatters, extracted from the melt pool images for the high
 431 VED conditions 2 and 3. The transversal X-CT cross-sections are shown as well revealing the
 432 sub-surface keyhole porosity below the line scan. For condition 2, a keyhole pore is only formed
 433 at the end of the scan. This is in agreement with the observations of other authors [33], where the
 434 rapid collapse of the melt pool at the end of a track is associated with the formation of keyhole
 435 porosity. A keyhole at the end of the track can also be observed for condition 3. In both cases,
 436 the melt pool collapse can be associated with a spatter ejection. These observations confirm that
 437 the rapid melt pool closure on laser turn-off and galvanometer scanner deceleration is associated
 438 with keyhole porosity and spatter ejection, but furthermore, that these spatters are successfully
 439 detected by the algorithm applied to the camera images.

440 Next to the keyhole at the end of the track, many more keyholes and significant spattering can be
441 detected all along the track in the coaxial camera images for condition 3 (Figure 12). To further
442 demonstrate the correlation between the formation of keyhole porosity and the presence of
443 spatters, the subsequent binary melt pool images processed with the above described algorithm
444 are shown in Figure 13 (condition 2) and 14 (condition 3). For condition 2, only 1 spatter event is
445 seen in the last images. For condition 3, numerous spatters are observed over the entire length of
446 the scan (for instance in the first image at 8.75 mm and last image at 9 mm in Figure 14), which
447 might indicate a possible correlation with the many keyhole pores observed by X-CT for this
448 sample.



449

450 **Figure 13.** The evolution of the binarized melt pool images captured for the Position Y of 6.96
451 mm to 7.5 mm of the line scan with condition 2 ($P = 340 \text{ W}$, $v = 1000 \text{ mm.s}^{-1}$).



452

453

454

Figure 14. The evolution of the binarized melt pool images captured for the Position Y of 8.74 mm to 9 mm of the line scan with condition 3 ($P = 170 \text{ W}$, $v = 500 \text{ mm.s}^{-1}$).

455

456

457

458

459

460

461

462

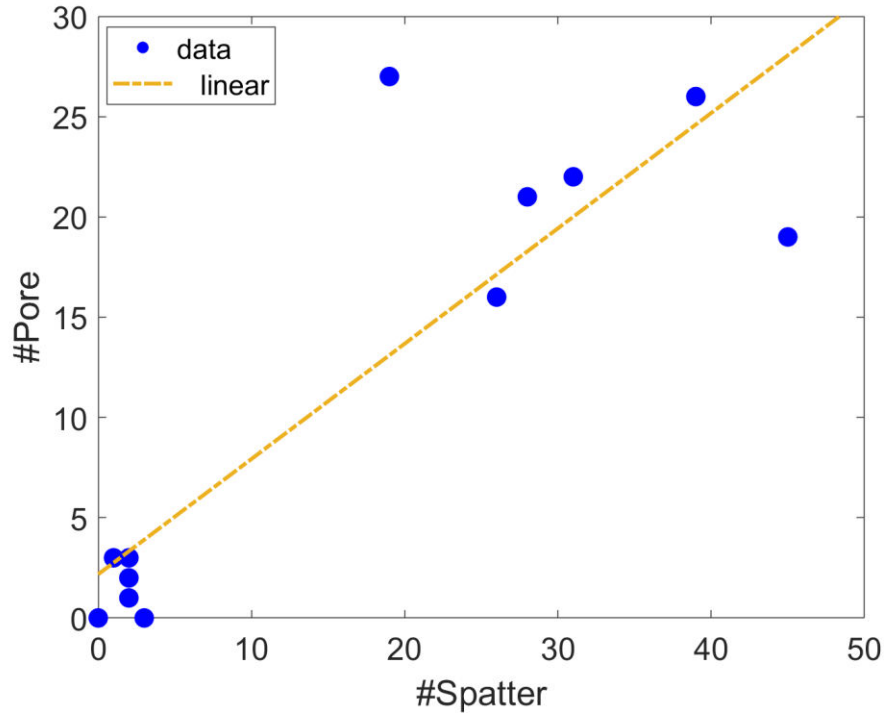
463

464

465

466

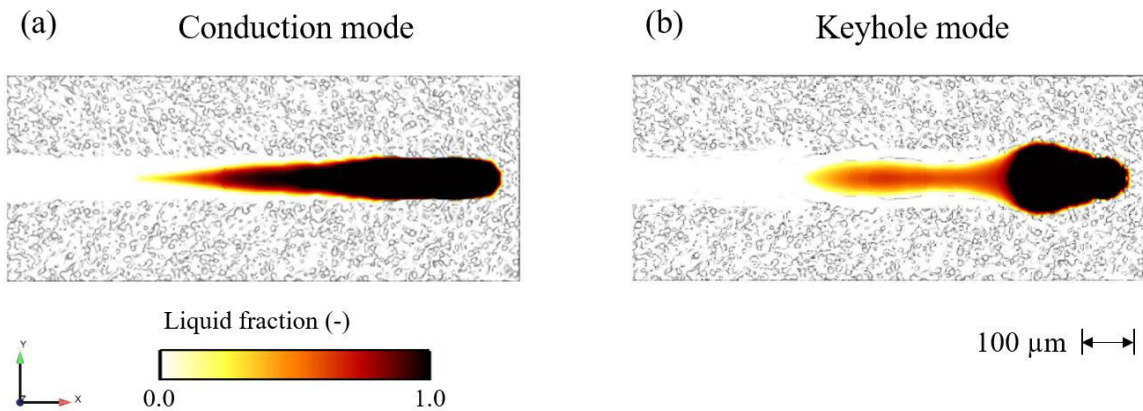
To further investigate a possible correlation between the presence of spatters and the formation of keyhole pores, the melt pool images and the X-CT cross-section images of 12 line scans with high VED (condition 2 and 3) have been further processed and analysed. The analysis is performed from the start until the end of a single track with an analysis resolution of $100 \mu\text{m}$. This means that if there are multiple spatters detected within a $100 \mu\text{m}$ range, they are counted as a single spatter event. Figure 15 shows a correlation between the number of keyhole pores observed in the X-CT cross-section images and the number of the spatter events for all the line scans of condition 2 and 3. The horizontal axis of the plot represents the number of spatter events detected in the coaxial melt pool images, while the vertical axis represents the number of keyhole pores detected in the X-CT cross-section images. It is clear from Figure 15 that the number of spatter events correlates with the number of observed keyhole pores along the Ti-6Al-4V tracks studied in this work.



467 **Figure 15.** Correlation between the number of keyhole pores detected with the X-CT and the
 468 number of spatters detected with the camera images processed with the proposed algorithm
 469 obtained from the 12 line scans with high VED (condition 2 and 3). Pearson's linear correlation
 470 coefficient of such a relationship is 0.87.

471 3.3 Finite Volume Model of the melt pool

472 With the melt pool monitoring system used in the previous sections, we can get information on
 473 spatter and melt pool width and length, but it is not possible to observe the melt pool depth. CFD
 474 simulations were therefore performed to get more insight in the dimensional evolution of all melt
 475 pool dimensions. The CFD simulation has been performed for two experimental conditions
 476 (condition 1: $P = 170 \text{ W}$, $v = 1000 \text{ mm}\cdot\text{s}^{-1}$ and condition 3: $P = 170 \text{ W}$, $v = 500 \text{ mm}\cdot\text{s}^{-1}$). The
 477 computational domain is composed of 6,288,368 cells with an average size of $3.3 \mu\text{m}$. The cells
 478 are chosen with an aspect ratio very close to unity, which is preferred for surface-tracking
 479 algorithms. Top views of the simulated melt pool liquid fraction for both conditions are shown in
 480 Figure 16 (a) and (b). According to Figure 16 (a), the melt pool in the conduction mode is found
 481 to be in a stable condition due to its optimum VED level. In this case, the evaporation recoil
 482 pressure is not significant and thus the melt pool will not face any instability and will preserve its
 483 morphology as it moves along the track.



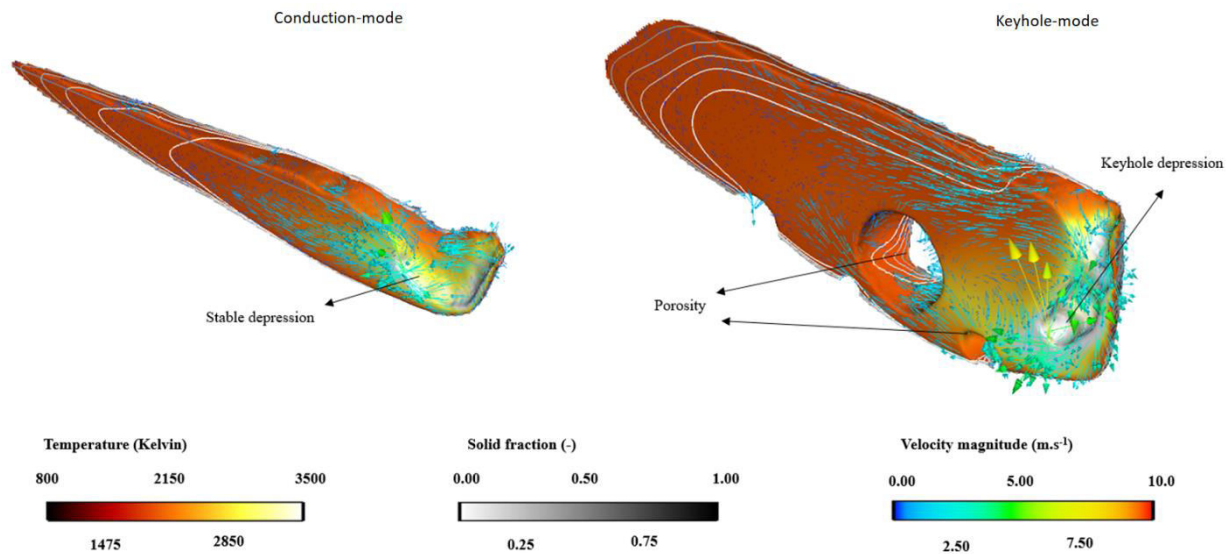
484

485 **Figure 16.** The top surface of the melt pool after reaching the centre of the computational
 486 domain during the scanning of the single-tracks along with the liquid fraction contour for
 487 optimum condition (a) $1000 \text{ mm}\cdot\text{s}^{-1}$ and keyhole condition (b) $500 \text{ mm}\cdot\text{s}^{-1}$.

488 Based on Figure 16 (a) and (b), the melt pool in the conduction mode (optimum VED) is
 489 narrower and at the same time longer from the top view as compared to the melt pool in the
 490 keyhole mode (high VED). The melt pool in the keyhole condition is highly unstable and the
 491 depression zone fluctuates due to the competition of recoil pressure and surface tension. At the
 492 same time, the Marangoni effect is more pronounced in the keyhole condition, mainly due to
 493 higher temperature gradient levels. This effect will make the melt pool in the keyhole mode
 494 wider than in the conduction mode that has lower temperature gradients, thus less pronounced
 495 Marangoni effect. Based on Figure 16, the melt pool in keyhole mode is shorter and at the same
 496 time wider, compared to the conduction mode.

497 A more detailed modelled view of the melt pool's internal structure for both of the studied cases
 498 is given in Figure 17. According to Figure 17, it is noted that most of the melt pool in keyhole
 499 mode is situated substantially below the top surface of the bulk domain. Accordingly, the melt
 500 pool is observed to be shorter from the top view, as compared to the conduction mode. The melt
 501 pool, however, becomes a lot deeper in the keyhole mode as compared to the conduction mode.
 502 This depth cannot be observed in our in-process experiments. While the comparison between the
 503 top view results from the numerical model and the experiments show qualitative agreement, the
 504 melt pool geometry is however found to be smaller in the experiments. This can be due to the
 505 fact that in the numerical model, the effect of gas-phase and its possible effect on the laser beam
 506 attenuation is not considered. More importantly, the discrepancy can be attributed to the fact that
 507 in the experiments, the monitoring device cannot accurately locate the solidus line from the melt
 508 pool tail, mainly due to low radiation of this zone. In this respect, the melt pool length is
 509 underestimated in the experiments as compared to the numerical model.

510 It is found in previous work [12] that keyhole porosities can still travel, disappear or combine
 511 with other pores after formation, indicating that it proves very difficult to correlate melt pool
 512 signatures at a certain location with pores formed below. A correlation between the total number
 513 of spatter as seen from melt pool images and the total number of pores in a line of a certain
 514 length, as shown in Figure 15, is however still possible.



515

516 **Figure 17.** Melt pool anatomy after reaching the centre of the computational domain for
 517 optimum condition (left) with scan speed $1000 \text{ mm}\cdot\text{s}^{-1}$, and keyhole condition (right) with scan
 518 speed $500 \text{ mm}\cdot\text{s}^{-1}$.

519 3.4 Microscopy evaluation of geometrical melt pool features

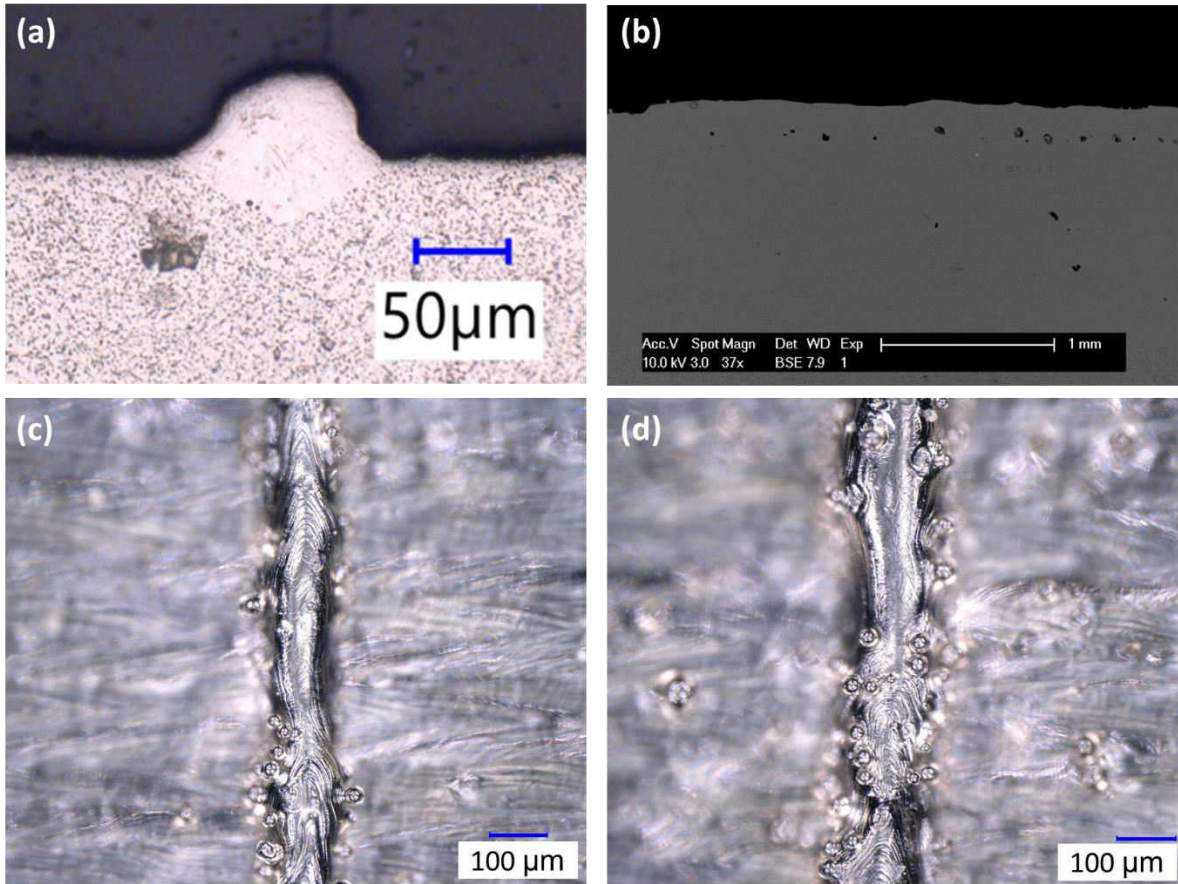
520 The melt pool depth and width are measured on samples of tracks produced with the optimum
 521 condition and the high VED condition. A total of 5 measurements are made for each dimension.
 522 The melt pool width is measured by imaging the top surface (Figure 18 (c) and (d)) by means of
 523 a Keyence VHX-600 optical microscope. The melt pool depth for the sample produced with high
 524 VED (condition 3) is estimated by examining the keyhole porosity depth on a polished cross
 525 section by using SEM (Figure 18 (b)). As the sample produced with optimum VED (condition 1)
 526 shows no porosity to help determine the melt pool depth, the depth for this condition is estimated
 527 by examining the melt pool for a single line scan performed on a cold-rolled Ti-6Al-4V substrate
 528 [34]. The substrate is covered with a single layer of powder to mimic processing conditions. This
 529 experiment was carried out on a Concept Laser M1 LPBF machine, with similar VED to that for
 530 the optimum conditions. The laser power was set at 189 W, the scan speed at 900 mm/s. The
 531 laser beam spot size was $50 \mu\text{m } \varnothing_{1/e^2}$, resulting in a VED of $140 \text{ J}\cdot\text{mm}^{-3}$. A relevant cross-
 532 section is shown in Figure 18 (a) revealing a conduction-controlled melt pool, made possible by
 533 a difference in microstructure between the substrate and the line scan, readily revealing the melt
 534 pool boundaries. A summary of the measurement result is shown in Table 4. For optimum VED,
 535 a depth-to-width ratio (aspect ratio) of ~ 0.85 is observed, indicating conduction-controlled
 536 melting. For the high VED, a depth-to-width ratio (aspect ratio) of ~ 2.4 is observed, indicating
 537 keyhole mode melting. The melt pool width values from Table 4 are smaller than those
 538 determined from the coaxial camera images (Table 3). Future work will focus on the calibration
 539 of melt pool grey-level that leads to the same camera melt pool width as the measured track
 540 width.

541

542

Table 4. Melt pool dimensions for optimal (condition 1) and high VED (condition 3).

Optimum VED (condition 1, $\nu = 1000 \text{ mm}\cdot\text{s}^{-1}$)			High VED (condition 3, $\nu = 500 \text{ mm}\cdot\text{s}^{-1}$)		
Depth / μm	Width / μm	Depth-to-width ratio	Depth / μm	Width / μm	Depth-to-width ratio
77 ± 2	90 ± 9	0.85	198 ± 9	82 ± 13	2.4



543

544 **Figure 18.** Melt pool geometrical features for Ti-6Al-4V scan track, (a) Melt pool cross-section
 545 perpendicular to the line track, produced on a cold-rolled Ti-6Al-4V substrate with a VED of 140
 546 $\text{J}\cdot\text{mm}^{-3}$, similar to condition 1 (Optimum VED); (b) SEM of melt pool cross-section parallel to
 547 the line track for the sample of condition 3 (High VED); (c) Top view of the line track with
 548 Optimum VED (condition 1); (d) Top view of the line track with High VED (condition 3).

549 4. Conclusion

550 The melt pool intensity and geometry for single tracks melted upon an LPBF substrate are
 551 recorded and analysed using coaxial camera melt pool monitoring. Line scans are printed with
 552 optimum, low and high volumetric energy density (VED). Extensive keyhole formation was

553 observed for the lines printed with high VED at reduced speed. While the average melt pool
554 intensity is the highest for the high VED condition at high speed, the integrated melt pool
555 intensity over print time for a certain line length is the highest for the high VED condition at low
556 speed. These results could indicate that the occurrence of keyhole mode melting is tied with the
557 integrated average of the melt pool radiation, while simultaneously being less dependent on the
558 average measured radiation. Next, image processing and features extraction steps for
559 characterising the melt pool geometry and spatters were applied to the coaxial camera images.
560 Contrary to expectations, no significant difference in the melt pool area, width and length is
561 observed between the optimum and keyhole mode conditions. Also, spatters originating from the
562 melt pool were analysed and counted by using an image processing algorithm for coaxially
563 acquired camera images. For a certain line length, a correlation between the number of keyhole
564 pores and the number of spatter was found, indicating that spatter could be another important in-
565 process signature of keyhole formation.

566 CFD simulations provide more insights into the melt pool evolution and keyhole pore formation.
567 From those simulations, it looks like the melt pool depths for the optimum and the keyhole
568 process are very different. The high VED process at low speed shows a very deep melt pool
569 depth possibly leading to keyhole formation and the optimum process only shows a shallow melt
570 pool depth. The increase in melt pool depth over melt pool width ratio for the high VED
571 condition at low speed was confirmed by measuring scan track depth and width of line scan
572 samples.

573 While this work shows that evaluating the integrated melt pool intensity over print time for a
574 certain line length and detecting spatter could play an important role in assessing the quality of a
575 printed part, building a complete quality assurance system for metal printing will require more
576 research where approaches similar to the one proposed in this paper are needed to get a full
577 understanding of the metal melting process including other types of metal printing defects. The
578 authors will continue their research in this area and extend the proposed approach with more
579 process information to build up a more complete picture of the defect formation process.

580 **5. Acknowledgement**

581 This research work was funded by research project “PAM² (Precision Additive Metal
582 Manufacturing)” of the EU Framework Programme for Research and Innovation within Horizon
583 2020 - Marie Skłodowska-Curie Innovative Training Networks under grant agreement No
584 721383 and by the agency Flanders Innovation & Entrepreneurship (VLAIO) through the
585 Flanders Make project MONICON ICON (HBC.2016.0459). The authors acknowledge Prof.
586 Shoufeng Yang (KU Leuven) for initial supervision and discussion of this work.

587 **6. Statements and Declarations**

588 **6.1 Funding**

589 This research work was funded by research project “PAM² (Precision Additive Metal
590 Manufacturing)” of the EU Framework Programme for Research and Innovation within Horizon
591 2020 - Marie Skłodowska-Curie Innovative Training Networks under grant agreement No

592 721383 and by the agency Flanders Innovation & Entrepreneurship (VLAIO) through the
593 Flanders Make project MONICON ICON (HBC.2016.0459).

594 **6.2 Conflicts of interest/Competing interests**

595 The authors have no conflict of interest to declare.

596 **6.3 Availability of data and material**

597 Not applicable

598 **6.4 Code availability**

599 Not applicable

600 **6.5 Ethics approval**

601 Approved

602 **6.6 Consent to participate**

603 The authors provide consent to participate.

604 **6.7 Consent for publication**

605 The authors give consent for publication.

606 **6.8 Authors' contributions**

607 **Aditi Thanki:** Conceptualization, investigation, formal analysis, visualization, validation,
608 writing – original draft. **Louca Goossens:** Conceptualization, formal analysis, writing – review
609 and editing. **Agusmian Partogi Ompusunggu:** Conceptualization, supervision, investigation,
610 formal analysis, software, writing – original draft. **Mohamad Bayat:** Investigation, formal
611 analysis, writing – original draft. **Abdellatif Bey-Temsamani:** Project management, writing –
612 original draft. **Brecht Van Hooreweder:** Supervision, resources, writing – review and editing.
613 **Jean-Pierre Kruth:** Resources, writing – review and editing. **Ann Witvrouw:**
614 Conceptualization, supervision, funding acquisition, resources, project management, writing –
615 original draft.

616 **7. References**

- 617 1. Kruth J-P, der Schueren B (1995) Direct production of metallic parts by rapid prototyping.
618 In: Proceedings of the 12th International Congress Laser. pp 123–134
- 619 2. Meiners W (1999) Direktes Selektives Laser Sintern einkomponentiger metallischer
620 Werkstoffe, RWTH Aachen. Dissertation
- 621 3. Li C, Pisignano D, Zhao Y, Xue J (2020) Advances in medical applications of additive
622 manufacturing. Engineering

- 623 4. Abe F, Osakada K, Shiomi M, et al (2001) The manufacturing of hard tools from metallic
624 powders by selective laser melting. *Journal of Materials Processing Technology* 111:210–
625 213. [https://doi.org/10.1016/S0924-0136\(01\)00522-2](https://doi.org/10.1016/S0924-0136(01)00522-2)
- 626 5. Leal R, Barreiros FM, Alves L, et al (2017) Additive manufacturing tooling for the
627 automotive industry. *The International Journal of Advanced Manufacturing Technology*
628 92:1671–1676
- 629 6. Liu R, Wang Z, Sparks T, et al (2017) Aerospace applications of laser additive
630 manufacturing. In: *Laser additive manufacturing*. Elsevier, pp 351–371
- 631 7. Rombouts M, Kruth JP, Froyen L, Mercelis P (2006) Fundamentals of selective laser
632 melting of alloyed steel powders. *CIRP Annals - Manufacturing Technology* 55:187–192.
633 [https://doi.org/10.1016/S0007-8506\(07\)60395-3](https://doi.org/10.1016/S0007-8506(07)60395-3)
- 634 8. Zhang B, Li Y, Bai Q (2017) Defect formation mechanisms in selective laser melting: a
635 review. *Chinese Journal of Mechanical Engineering* 30:515–527
- 636 9. Khairallah SA, Anderson AT, Rubenchik A, King WE (2016) Laser powder-bed fusion
637 additive manufacturing: Physics of complex melt flow and formation mechanisms of
638 pores, spatter, and denudation zones. *Acta Materialia* 108:36–45
- 639 10. Ranjan R, Yang Y, Ayas C, et al (2017) Controlling local overheating in topology
640 optimization for additive manufacturing. In: *Proceedings of euspen special interest group
641 meeting: additive manufacturing, Leuven, Belgium*
- 642 11. King WE, Barth HD, Castillo VM, et al (2014) Observation of keyhole-mode laser
643 melting in laser powder-bed fusion additive manufacturing. *Journal of Materials
644 Processing Technology* 214:2915–2925
- 645 12. Bayat M, Thanki A, Mohanty S, et al (2019) Keyhole-induced porosities in Laser-based
646 Powder Bed Fusion (L-PBF) of Ti6Al4V: High-fidelity modelling and experimental
647 validation. *Additive Manufacturing* 30:. <https://doi.org/10.1016/j.addma.2019.100835>
- 648 13. Matsunawa A, Kim J-D, Seto N, et al (1998) Dynamics of keyhole and molten pool in
649 laser welding. *Journal of laser applications* 10:247–254
- 650 14. Martin AA, Calta NP, Khairallah SA, et al (2019) Dynamics of pore formation during
651 laser powder bed fusion additive manufacturing. *Nature communications* 10:1–10
- 652 15. Cunningham R, Zhao C, Parab N, et al (2019) Keyhole threshold and morphology in laser
653 melting revealed by ultrahigh-speed x-ray imaging. *Science* 363:849–852
- 654 16. Everton SK, Hirsch M, Stavroulakis PI, et al (2016) Review of in-situ process monitoring
655 and in-situ metrology for metal additive manufacturing. *Materials and Design*
- 656 17. Goossens LR, Van Hooreweder B (2021) A virtual sensing approach for monitoring melt-
657 pool dimensions using high speed coaxial imaging during laser powder bed fusion of

- 658 metals. Additive Manufacturing 40:101923
- 659 18. Matthews MJ, Guss G, Khairallah SA, et al (2016) Denudation of metal powder layers in
660 laser powder bed fusion processes. Acta Materialia 114:33–42
- 661 19. Ly S, Rubenchik AM, Khairallah SA, et al (2017) Metal vapor micro-jet controls material
662 redistribution in laser powder bed fusion additive manufacturing. Scientific reports 7:1–12
- 663 20. Gunenthiram V, Peyre P, Schneider M, et al (2018) Experimental analysis of spatter
664 generation and melt-pool behavior during the powder bed laser beam melting process.
665 Journal of Materials Processing Technology 251:376–386
- 666 21. Repossini G, Laguzza V, Grasso M, Colosimo BM (2017) On the use of spatter signature
667 for in-situ monitoring of Laser Powder Bed Fusion. Additive Manufacturing 16:35–48
- 668 22. Thanki A, Goossens L, Mertens R, et al (2019) Study of keyhole-porosities in selective
669 laser melting using X-ray computed tomography. 9th Conference on Industrial Computed
670 Tomography 1–7
- 671 23. Thorlabs (2017) Si Switchable Gain Detector User Guide. 15
- 672 24. Mikrotron GmbH (2016) High-Speed CMOS CameraEoSens®3CL Datasheet. 2
- 673 25. Lim JS (1990) Two-dimensional signal and image processing. ph
- 674 26. Lee J-S (1980) Digital image enhancement and noise filtering by use of local statistics.
675 IEEE transactions on pattern analysis and machine intelligence 165–168
- 676 27. Matas J, Chum O, Urban M, Pajdla T (2004) Robust wide-baseline stereo from maximally
677 stable extremal regions. Image and vision computing 22:761–767
- 678 28. Hu M-K (1962) Visual pattern recognition by moment invariants. IRE transactions on
679 information theory 8:179–187
- 680 29. Cho J-H, Na S-J (2006) Implementation of real-time multiple reflection and Fresnel
681 absorption of laser beam in keyhole. Journal of Physics D: Applied Physics 39:5372
- 682 30. Tan W, Bailey NS, Shin YC (2013) Investigation of keyhole plume and molten pool based
683 on a three-dimensional dynamic model with sharp interface formulation. Journal of
684 Physics D: Applied Physics 46:55501
- 685 31. Young ZA, Guo Q, Parab ND, et al (2020) Types of spatter and their features and
686 formation mechanisms in laser powder bed fusion additive manufacturing process.
687 Additive Manufacturing 36:101438
- 688 32. Wang D, Wu S, Fu F, et al (2017) Mechanisms and characteristics of spatter generation in
689 SLM processing and its effect on the properties. Materials & Design 117:121–130
- 690 33. Martin AA, Calta NP, Hammons JA, et al (2019) Ultrafast dynamics of laser-metal

- 691 interactions in additive manufacturing alloys captured by in situ X-ray imaging. *Materials*
692 *Today Advances* 1:100002
- 693 34. Coen V (2020) An analytical melt pool model for Laser-Powder Bed Fusion An
694 experimental approach for the validation and calibration of a model for Ti6Al4V powder.
695 KULeuven